RESEARCH ARTICLE

Key Points:
- Shock equation of state and melting curve of Fe-8 wt% Ni-10 wt% Si alloy were measured up to ~250 GPa by hypervelocity impacts with shock velocity, particle velocity, and temperature measurements
- An adiabatic temperature of ~3900 K and ~5300 K at the top and bottom of the Earth outer core, respectively, is estimated for Fe-5 wt% Ni alloyed with 6 wt% Si and 2 wt% S that matches the outer core's seismic profile sufficiently
- A modeled geotherm for a plausible Si-rich Fe alloy of the outer core suggests a thermal gradient of ~5.8–6.8 (±1.6) K/km in the D'' region and a likely high heat flow of 13–19 TW across the CMB

Supporting Information:
- Data Set S1

Correspondence to:
J.-F. Lin and T. Sekine,
afu@jsg.utexas.edu;
toshimori.sekine@hpstar.ac.cn

Shock Compression and Melting of an Fe-Ni-Si Alloy: Implications for the Temperature Profile of the Earth's Core and the Heat Flux Across the Core-Mantle Boundary

HPSTAR
527-2018

Youjun Zhang[1,2] [ID], **Toshimori Sekine[1,2], Jung-Fu Lin[1,3]** [ID], **Hongliang He[4], Fusheng Liu[5], Mingjian Zhang[5], Tomoko Sato[2], Wenjun Zhu[4],** and **Yin Yu[4]**

[1]Center for High Pressure Science and Technology Advanced Research (HPSTAR), Shanghai, China, [2]Department of Earth and Planetary Systems Science, Hiroshima University, Higashihiroshima, Japan, [3]Department of Geological Sciences, Jackson School of Geosciences, The University of Texas at Austin, Austin, TX, USA, [4]National Key Laboratory of Shock Wave and Detonation Physics, China Academy of Engineering Physics, Mianyang, China, [5]College of Physical Science and Technology, Southwest Jiaotong University, Chengdu, China

Abstract Understanding the melting behavior and the thermal equation of state of Fe-Ni alloyed with candidate light elements at conditions of the Earth's core is critical for our knowledge of the region's thermal structure and chemical composition and the heat flow across the liquid outer core into the lowermost mantle. Here we studied the shock equation of state and melting curve of an Fe-8 wt% Ni-10 wt% Si alloy up to ~250 GPa by hypervelocity impacts with direct velocity and reliable temperature measurements. Our results show that the addition of 10 wt% Si to Fe-8 wt% Ni alloy slightly depresses the melting temperature of iron by ~200–300 (±200) K at the core-mantle boundary (~136 GPa) and by ~600–800 (±500) K at the inner core-outer core boundary (~330 GPa), respectively. Our results indicate that Si has a relatively mild effect on the melting temperature of iron compared with S and O. Our thermodynamic modeling shows that Fe-5 wt% Ni alloyed with 6 wt% Si and 2 wt% S (which has a density-velocity profile that matches the outer core's seismic profile well) exhibits an adiabatic profile with temperatures of ~3900 K and ~5300 K at the top and bottom of the outer core, respectively. If Si is a major light element in the core, a geotherm modeled for the outer core indicates a thermal gradient of ~5.8–6.8 (±1.6) K/km in the D'' region and a high heat flow of ~13–19 TW across the core-mantle boundary.

1. Introduction

Based on several constraints from seismology, geochemical and cosmochemical considerations, and mineral physics, the Earth's core is composed of an Fe-Ni alloy with some small amounts of light element(s) such as Si, O, S, C, and H (Li & Fei, 2003; McDonough, 2003; Poirier, 1994). The presence of light elements in the core is known to affect iron's physical properties, including its seismic velocity-density profile, crystal structure, and melting behavior (Li & Fei, 2003). Knowledge of the Earth's core geotherm is critical for evaluating the evolution and energetics of the core and deep mantle, including the energy source for the geodynamo (Buffett, 2003; Nimmo, 2015). The temperature gradient across the core-mantle boundary (CMB) can be used to constrain the heat transfer between the lowermost mantle and core, as well as the melting behavior of mantle materials in the D'' region (Buffett, 2000; Labrosse, 2015; Lay et al., 2008; Van der Hilst et al., 2007). The temperature at the inner-core boundary (ICB) is anchored between the liquidus of the outer-core iron alloy and the solidus inner-core alloy and is vital for understanding the solidification, stratification, and growth of the inner core (Alboussiere et al., 2010; Gubbins et al., 2011).

Knowing the thermal structure and dynamic state of the Earth's core requires precise determination of the appropriate iron alloy composition's melting curve at the region's relevant pressure-temperature conditions. However, this has been a challenging task because of the extreme conditions required for these experiments and because obtaining accurate verification of electron correlations at very high pressure-temperature (*P-T*) with theoretical calculations is problematic. Thus far, numerous researchers have endeavored to measure or derive the melting temperature of pure Fe up to the ICB conditions

with shock wave and laser-heated diamond anvil cell (LHDAC) techniques (Anzellini et al., 2013; Aquilanti et al., 2015; Boehler, 1993; Brown & McQueen, 1986; Luo & Ahrens, 2004; Nguyen & Holmes, 2004; Williams et al., 1987; Yoo et al., 1993). Unfortunately, there is a wide range of results, likely due to technical difficulties in reliably detecting melting. A series of studies have reported the melting curve of Fe in LHDAC experiments through X-ray diffraction and diffuse scattering (Anzellini et al., 2013), shock wave experiments combined with Hugoniot, sound velocity, and Hugoniot temperature measurements (Brown & McQueen, 1986; Luo & Ahrens, 2004; Nguyen & Holmes, 2004; Tan et al., 2005), and first-principles computations (Alfè et al., 2002; Sola & Alfe, 2009). These studies all indicate a melting temperature of ~6200 (±500) K for pure iron at the ICB.

The melting temperatures of Fe alloyed with Ni and/or other candidate light elements like Si, S, O, and C were investigated previously and were recently reviewed (Fischer, 2016). Adding light elements into Fe likely reduces the melting temperature of pure Fe, but the magnitude of the effects differs for various light elements. However, most of these studies were conducted at low pressures relative to the core, and the results are extrapolated to the ICB conditions. Silicon (~6–10 wt% Si) has been commonly considered a dominant light element in the core (Hirose et al., 2013; Lin et al., 2002) due to its abundance in the silicate mantle (Allègre et al., 1995; McDonough, 2003), its high solubility in liquid iron (Takafuji et al., 2005), and the appropriate partitioning coefficient between molten iron and silicate melts (Ricolleau et al., 2011; Tsuno et al., 2013). In addition, there are likely iron-silicate chemical intersections at the CMB (Dubrovinsky et al., 2003; Knittle & Jeanloz, 1991). Further, the observed small isotopic differences between terrestrial samples and meteorites (Georg et al., 2007) are consistent with silica incorporation during the Earth's core formation. Si as a light element is also supported by recent measurements of density and sound velocity under core conditions, which are generally consistent with seismological data (Fischer et al., 2014; Lin, Campbell, et al., 2003; Lin, Struzhkin, et al., 2003; Liu et al., 2014, 2016; Mao et al., 2012; Zhang, Sekine, et al., 2016). Therefore, knowing the melting temperatures in the Fe-Ni-Si system at ICB pressures is critical for determining the thermal structure of the outer core.

Previous studies indicate that the presence of 5–10 wt% Ni in Fe does not significantly affect its density and sound velocity (Kantor et al., 2007) and Ni itself has similar melting temperatures to Fe at high pressures (Lord et al., 2014). However, Ni can change the *P–T* phase diagram of Fe (Dubrovinsky et al., 2007; Kuwayama et al., 2008; Sakai et al., 2011), which may affect its melting behavior. An Fe-10 wt% Ni alloy likely has slightly lower melting temperatures than pure Fe up to ~100 GPa (Zhang, Jackson, et al., 2016). The melting temperatures of Fe and Fe-Ni samples with 9–18 wt% Si at high pressures were investigated with in situ X-ray diffuse scattering in an LHDAC (Fischer et al., 2012, 2013; Morard et al., 2011) and by observing recovered samples (Asanuma et al., 2010). Although their experimental conditions were mostly below the CMB pressure, a significant depression of the melting temperature was observed in the samples with a high Si content (~16–18 wt%; Asanuma et al., 2010; Fischer et al., 2012; Morard et al., 2011). However, inconsistent melting temperatures are reported for samples with a low Si content (~9–10 wt%) such as Fe-9 wt% Si and Fe-5 wt% Ni-10 wt% Si (Fischer et al., 2013; Morard et al., 2011). The Fe-9 wt% Si system even shows a higher melting temperature than pure iron at the CMB (Fischer et al., 2013). Therefore, more experiments on melting temperatures are required to resolve this fundamental issue, especially for samples with ~6–10 wt% Si, which correspond closely to previously reported core composition models.

The density and sound velocity of Fe-9 wt% Ni-10 wt% Si melt have been measured up to ~280 GPa using a shock wave method, and the results were found to match well with the seismological observations of the outer core (Zhang, Sekine, He, Yu, et al., 2014; Zhang, Sekine, et al., 2016). In order to understand the core's thermal structure further, direct measurements of this composition's Hugoniot temperatures are required as a function of pressure. Here we conducted high-velocity impact experiments for a model core composition of a homogeneous Fe-8 wt% Ni-10 wt% Si alloy (hereafter Fe-8Ni-10Si). We measured its densities and temperatures up to ~255 GPa and ~237 GPa, respectively, under shock loading. The melting temperature of Fe-8Ni-10Si was determined by Hugoniot temperature measurements, and the temperature at the ICB pressure was estimated. By combining the melting temperatures of Fe, Fe-S, and Fe-O alloys, an adiabatic thermal state for a Si-rich Fe-Ni compositional model was derived for outer core pressures. Finally, the melting behavior of the Fe-Ni-Si alloy and the heat flow across the CMB were further constrained based on our measured results and thermodynamic modeling.

2. Material and Experimental Procedure

2.1. Starting Material

Highly homogeneous samples are required to reliably measure shock temperatures and for determining the thermal equation of state. We synthesized chemically homogeneous samples of an Fe-8Ni-10Si alloy ($Fe_{74.9}Ni_{6.9}Si_{18.2}$ in atomic percent) at ~1100°C under a pressure of 20 MPa by sintering an alloyed powder from Kojundo Chemicals, Japan. The grain sizes remained ~10–80 μm (Figures 1a–1d) after sintered. The average density of the synthesized sample measured by the Archimedean method was 7.352 ± 0.005 g/cm^3, which is denser than a previously sintered sample of Fe-9Ni-10Si alloy mixture (6.853 ± 0.036 g/cm^3) that consisted of mixed phases of Fe_3Si, FeNi, and FeNiSi (Zhang, Sekine, He, Yu, et al., 2014). The longitudinal (V_l) and shear (V_s) velocities of Fe-8Ni-10Si determined by the pulse reflection method (Kono et al., 2007) were 6.064 and 3.123 km/s, respectively. The bulk sound velocity (V_b) at ambient conditions was 4.875 km/s by the equation $V_l^2 = V_b^2 + (4/3)V_s^2$.

We analyzed the specimen using an electron probe microanalyzer (JEOL JXA-8200 WD/ED) to determine its composition and chemical homogeneity. Backscattered electron images of the specimen are shown in Figures 1a–1d, and the compositions of the randomly selected points are listed in supporting information Table S1. These analyses show that the sample is very chemically homogeneous with an average composition of Fe-8.1(±0.1) wt% Ni-10.4(±0.1) wt% Si. X-ray diffraction patterns are also shown in supporting information Figure S1 as analyzed using Cu Kα radiation with a Rigaku MicroMax 007HF. Analysis of the X-ray diffraction spectra indicates that the starting sample can be well indexed by a face-centered cubic structure (Fm-3m) with a lattice parameter of 5.683 ± 0.001 Å at ambient conditions, corresponding to an initial density of 7.358 ± 0.004 g/cm^3, which is consistent with the value from the Archimedean method (7.352 ± 0.005 g/cm^3), indicating no porosity. The backscattered electron images show grain sizes around 50–100 μm, with trace black areas of SiO_2 (<0.1 wt%), and slight contrast variations due to the different crystal orientations. The initial density of the homogeneous Fe-8Ni-10Si alloy is consistent with those of Fe-Si alloys (Marsh, 1980) at ambient conditions (supporting information Figure S2). In addition, Fe-10 wt% Ni with an initial density of 7.886 g/cm^3 is only ~0.2% denser than the pure Fe (7.874 g/cm^3), confirming that adding 10% Ni into Fe does not increase the iron's density significantly. The density and bulk sound velocity of the present Fe-8Ni-10Si alloy are different from those measured from a previous Fe-9Ni-10Si (Zhang, Sekine, He, Yu, et al., 2014) because of the different phases present, despite having a very similar bulk chemical composition and no difference in porosity.

2.2. Hugoniot and Shock Temperature Measurements

We conducted shock experiments using a two-stage light-gas gun at the Southwest Jiaotong University, China. For the Hugoniot experiments, the impact velocity of the flyer and shock velocity of the Fe-8Ni-10Si alloy were measured with an electromagnetic method and electrical pins system, respectively (Zhang, Sekine, He, Yu, et al., 2014). The samples (17.0 mm diameter, 2.500 ± 0.005 mm thick) were polished on both surfaces to allow accurate measurements of their thicknesses using a micrometer. The measured impact velocity and shock velocity uncertainties were within ~0.5% and ~2%, respectively. The experimental conditions and results up to ~255 GPa are listed in Table 1.

The schematic setup of the temperature measurement is illustrated in supporting information Figure S3. The interface temperatures between the Fe-8Ni-10Si alloy and the transparent window under a vacuum (< ~1 Pa) were measured using an optical pyrometer with 10 to 14 channels in the wavelength range of 400–800 nm, with a narrow band width filter of 10–30 nm and a ~3 ns time resolution (Zhou et al., 2015). The thermal radiation emitted from the Fe-Ni-Si alloy/window interface was collected through optical fibers to transmit the signals to the pyrometer. The pyrometer consists of photomultiplier tubes that give voltages corresponding to the emission strength as oscillographs. Single-crystal lithium fluoride (LiF) 20 mm in diameter and 5 mm thick with (100) orientation was used as the window material, which is transparent up to ~200 GPa. In order to avoid possible strong scattering of the emitted light, black masks were put on the surface and edge of the LiF window, except the central area where the fiber was located (as illustrated in supporting information Figure S3), so that only light from the center of the interface was collected through the optical fiber. The samples were finely polished to a mirror finish on both surfaces to contact firmly with the window by prepressing force (Hao et al., 2007). This special sample configuration avoids effects on the spectral radiation from the
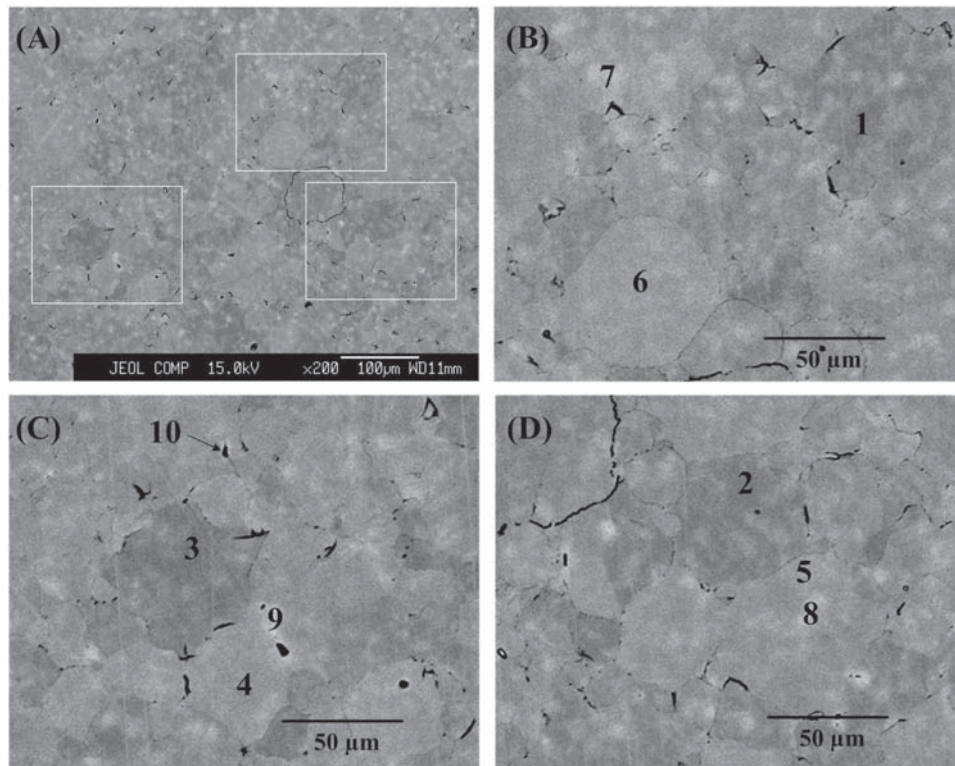
Figure 1. Backscattered electron images of the starting Fe-8Ni-10Si alloy. Numbers correspond to the randomly selected points for the compositional analyses by electron probe microanalyzer. The analysis is tabulated in supporting information Table S1.

surface gap between the sample and window, which would produce an initial "sharp peak" and result in a false high-temperature thin layer (Huang et al., 2010).

Each channel of the pyrometer was calibrated by the spectral radiance from a tungsten-halogen (WBr) standard lamp before each shot (pre-shot), and the measured voltages were converted into light flux based on their calibration. Pyrometer experiments were performed up to a Hugoniot pressure of ~237 GPa, and the impact conditions are listed in Table 2. Digital oscilloscopes with a sampling rate of 3.5 GHz recorded the spectral data.

3. Experimental Results

3.1. Hugoniot Equation of State of Fe-8Ni-10Si Alloy

The shock velocity-particle velocity (U_s-u_p) and pressure-density (P-ρ) relations of Fe-8Ni-10Si were obtained by the impedance-matching method as shown in Figures 2A and 2B, respectively. A linear relationship

Table 1
Impact Conditions and Results of the Hugoniot Density Measurements of the Fe-8Ni-10Si Alloy

Shot no./flyer[a]	V_{imp} (km/s)	ρ_0 (g/cm^3)	U_s (km/s)	u_p (km/s)	P_H (GPa)	ρ (g/cm^3)
C1/Ta	2.93 (0.01)	7.346	7.33 (0.06)	1.76 (0.01)	94.8 (0.9)	9.67 (0.11)
C2/Ta	3.98 (0.01)	7.350	8.25 (0.08)	2.38 (0.01)	144.3 (1.5)	10.33 (0.14)
C3/Ta	4.38 (0.01)	7.348	8.67 (0.05)	2.61 (0.01)	166.3 (1.2)	10.51 (0.08)
C4/Ta	5.05 (0.02)	7.363	9.20 (0.05)	3.01 (0.01)	203.9 (1.3)	10.94 (0.08)
C5/W	5.40 (0.02)	7.382	9.90 (0.15)	3.49 (0.02)	255.0 (4.1)	11.40 (0.2)

Note. V_{imp} is the impact velocity; ρ_0 is the initial density measured by the Archimedean method; U_s is the measured shock velocity; P_H is the Hugoniot pressure; and ρ is the Hugoniot density.
[a]The Hugoniot relations were used as flyers: Ta, ρ_0 = 16.68 g/cm^3, U_s = 3.293 + 1.307 u_p (km/s); W, ρ_0 = 19.25 g/cm^3, U_s = 3.935 + 1.578 u_p (km/s).

Table 2
Impact Conditions and Shock Temperatures Measured at the Interface Between the Fe-8Ni-10Si Alloy and the Single-Crystal LiF Window

Shot no.	Flyer/baseplate (mm)	Sample thickness (mm)	V_{imp} (km/s)	P_H (GPa)	P_R (GPa)	T_I (K)	ε
D1	1.5 W/1.0 sus304	2.4	4.11 (0.02)	167 (2)	93 (1)	3182 (121)	0.231 (0.061)
D2	1.5 Ta/1.0 sus304	2.0	4.48 (0.02)	171 (2)	95 (1)	3358 (55)	0.205 (0.023)
D3	1.5 Ta/1.0 sus304	2.0	5.15 (0.03)	210 (3)	116 (1)	4300 (140)	0.255 (0.04)
D4	1.5 Ta/1.0 sus304	2.0	5.59 (0.03)	237 (3)	131 (2)	5369 (80)	0.277 (0.021)

Note. V_{imp} = impact velocity; P_H = Hugoniot pressure; P_R = partially released pressure at the interface; and ε = emissivity.

between U_s and u_p can be fitted by U_s (km/s) = $C_0 + su_p$, where C_0 = 4.75 ± 0.09 and s = 1.48 ± 0.03. The fitted C_0 is close to the ambient bulk sound velocity of 4.875 km/s. The P-ρ relation is plotted by $P = \rho_0 C_0^2 (1 - \rho_0/\rho)/(1 - s(1 - \rho_0/\rho))^2$ as shown in Figure 2B. However, Fe-8Ni-10Si (red solid circles) is slightly denser by ~1% than Fe-9Ni-10Si in a liquid state (red open circles) at a pressure of ~250 GPa. The main reason for the density difference at high P-T is likely caused by the difference in the two samples' shock temperatures due to their initial densities. We should note that the measured Hugoniot density has an uncertainty of ~1% at very high pressures. The presence of an SiO_2 impurity (0.3–0.5 wt%) in the Fe-9Ni-10Si alloy mixture used by Zhang, Sekine, He, Yu, et al. (2014) can also contribute to the density difference, but this small impurity is likely too small to account for the density difference. Our present results using a single-phase Fe-Ni-Si alloy as the starting sample should represent a more reliable measurement of the Fe-Ni-Si alloy equation of state at relevant P-T conditions of the Earth's core.

3.2. Hugoniot Temperature of Fe-8Ni-10Si Alloy

The measured time-resolved thermal emission spectra are shown in Figure 3. Sudden voltage jumps are seen at point A, indicating the arrival of a shock wave at the interface, and then the sample reaches a compressed state before the rarefaction wave arrives at point C (Figure 3). We did not see any strong and sharp peaks caused by a possible mechanical gap between the sample and the LiF window. This observation confirms the firm contact condition between our sample and the LiF (Hao et al., 2007). We took the voltage amplitude (h) for each channel at a time of ~50 ns after the shock wave arrived at the interface, where the spectra plateau shows an equilibrium for each profile (crossover point of the spectra profile with a vertical dashed line in Figure 3). The experimental spectral radiation intensity (I_{exp}) was obtained based on the measured ratio of h to h_0 (the voltage amplitude in pre-shot calibration):

$$h/h_0 = 2\pi(1 - \cos\alpha_0)(I_N/I_0)^2(R/R_0)(I_{exp}/N_r) \qquad (1)$$

where N_r is the spectral radiation intensity of the standard lamp (WBr) and I_N and I_0 are the distance from the standard lamp to the head of the optical fiber for the standard lamp calibration and each pre-shot calibration, respectively. Usually, we use the same I_0 and I_N. R and R_0 are the load resistances during the pre-shot calibration and experiments, respectively. Here we used R = 50 Ω and R_0 = 10 kΩ. Each optical fiber has a 0.275 numerical aperture (sin α_0) and a 62.5 μm silica core (Zhou et al., 2015).

The interface temperature (T_I) and the emissivity (ε) at the partially released interface pressure (P_R) were obtained by fitting the measured spectral radiation intensities using Planck's equation of gray-body radiation for temperature (T) and wavelength (λ):
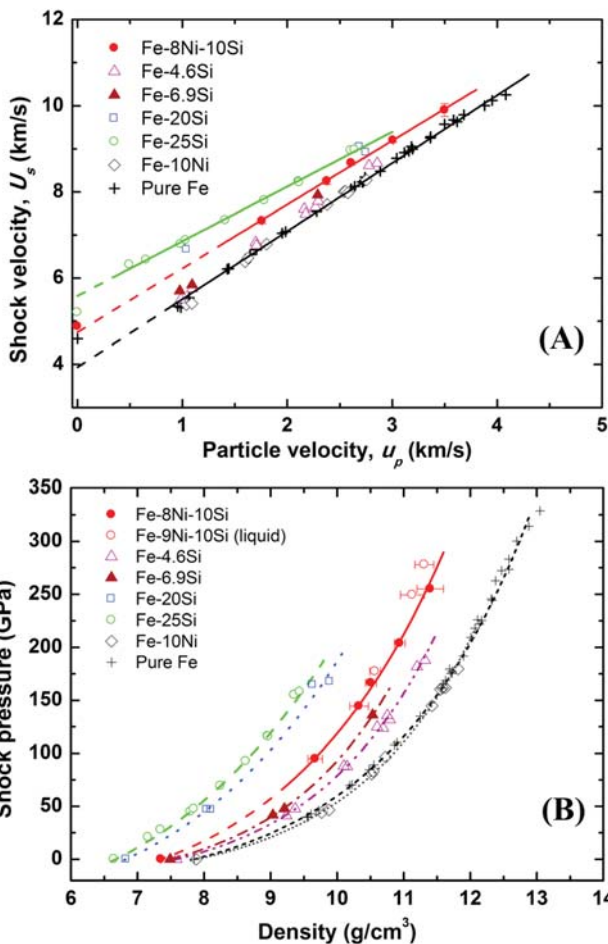

Figure 2. (a) The relationship between the shock velocity and particle velocity and (b) between the shock pressure and Hugoniot density of iron and its alloys. Previous shock wave measurements are also plotted for comparison. Data are the Fe-8Ni-10Si alloy (red solid circles; in this study); Fe-9Ni-10Si in liquid state (red open circles; Zhang, Sekine, He, Yu, et al., 2014); pure Fe (plus signs; Brown et al., 2000); and alloys of Fe-10Ni (dark green open diamonds), Fe-4.6Si (purple open triangles), Fe-6.9Si (wine solid triangles), Fe-20Si (blue open squares), and Fe-25Si (green open circles; Marsh, 1980).
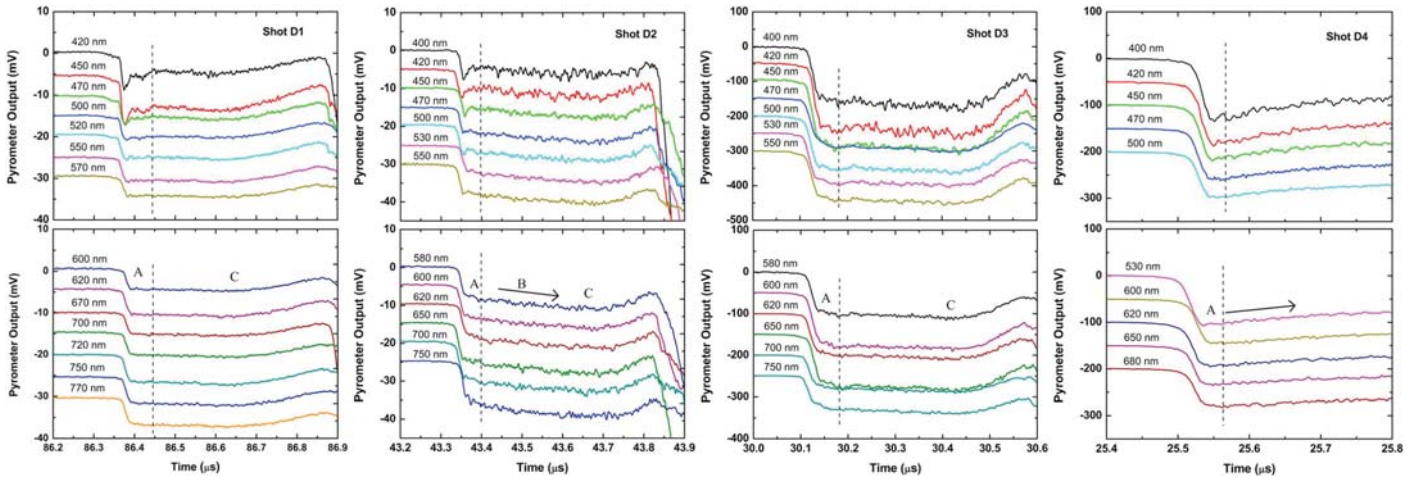
Figure 3. Time-resolved thermal emission spectra from the interface between the Fe-8Ni-10Si alloy and LiF window under shock loading. The spectra were collected using a photomultiplier tube system.

$$I_{\exp}(\lambda, \varepsilon, T) = \varepsilon \cdot C_1 \lambda^{-5}[\exp(C_2/\lambda T) - 1]^{-1} \qquad (2)$$

where C_1 and C_2 are the first and second radiation constants in Planck's radiation formula, with values of 1.191×10^{-16} W m^2 Sr^{-1} and 1.439×10^{-2} m K, respectively. Figure 4 shows the fitting of the spectral radiances versus wavelength in the gray-body model of Fe-8Ni-10Si. The results of the fitted T_I and ε are listed in Table 2.

The Hugoniot temperatures (T_H) of Fe-8Ni-10Si can be derived from the T_I, assuming an isentropic release, by the equation
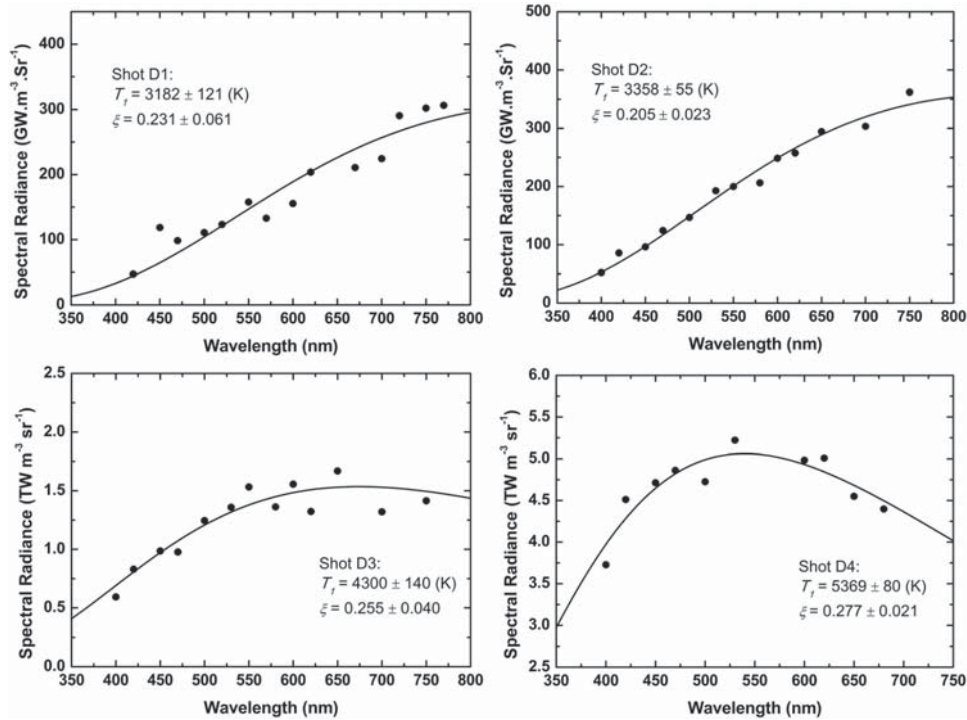

Figure 4. Spectral radiances of the shocked Fe-8Ni-10Si alloy as a function of wavelength. The spectra of shots D1 to D4 are fitted to Planck's radiation function to derive the Hugoniot temperatures.

Table 3
The Melting and Hugoniot Temperatures of the Fe-8Ni-10Si Alloy

Shot no.	T_W at P_R (K)	K_W at P_R (W/m/K)	K_S at P_R (W/m/K)	α	T_R at P_R (K)	T_m at P_R (K)	T_H at P_H (K)	T_m at P_H (K)
D1	1700 (100)	5.3 (0.3)	100 (20)	5.04 (0.8)	3476 (145)	3329 (176)	4045 (208)	—
D2	1750 (100)	5.2 (0.3)	100 (20)	5.08 (0.8)	3675 (114)	3517 (152)	4280 (188)	4280 (188)
D3	2350 (150)	4.0 (0.3)	120 (30)	6.01 (1.1)	4625 (227)	—	5390 (272)	—
D4	2750 (150)	3.5 (0.3)	140 (30)	6.09 (1.2)	5799 (198)	—	6720 (330)	—

Note. T_W is the temperature of LiF window at the partially released interface pressure (P_R); T_R is the temperature of the sample at P_R; T_H is the Hugoniot temperature at Hugoniot pressure (P_H); and K_W and K_S are the thermal conductivities of the LiF window and sample, respectively.

$$T_H = T_R \exp\left[\int_{V_R}^{V_H}(-\gamma/V)dV\right] \tag{3}$$

where V_R and V_H are the volumes of the samples at the pressure P_R and at the Hugoniot pressure (P_H), respectively, γ is the Grüneisen parameter, and T_R is the release temperature of the sample at P_R. There is thermal conduction from the high-temperature sample to the interface during release shock propagation to reach P_R (Nellis & Yoo, 1990):

$$T_R = T_I + (T_I - T_W)/\alpha \tag{4}$$

α is defined as:

$$\alpha = \left[(\rho C\kappa)_S/(\rho C\kappa)_W\right]^{1/2} \tag{5}$$

where T_W is the LiF window temperature; the subscripts of S and W denote the sample and the window, respectively; and ρ, C, and κ represent the density, heat capacity, and thermal conductivity, respectively. The relationships between the T_H, T_R, and T_I are illustrated in supporting information Figure S4A, and the details are described elsewhere (Dai et al., 2009; Nellis & Yoo, 1990). We used the thermal conductivity of the Fe-(~10 wt%)Si system (κ_S) at high pressures and high temperatures from first-principle calculations (de Koker et al., 2012; Pozzo et al., 2012, 2014) and high-pressure experiments of electrical conductivity (Gomi et al., 2013, 2016; Seagle et al., 2013). The density, shock temperature (T_W), and thermal conductivity of the LiF window were previously determined in shocked states by experiments and calculations (Holland & Ahrens, 1998; Liu et al., 2015; Smirnov, 2011; Zhao et al., 2014). The obtained T_R and T_H values are given in Table 3.

The Hugoniot temperature for the solid Fe-8Ni-10Si alloy was calculated from a thermodynamic equation based on the measured Hugoniot parameters (Brown & McQueen, 1986; McQueen et al., 1970):

$$dT = -T(\gamma/V)dV + (1/2C_V)[(V_0 - V)dP + (P - P_0)dV] \tag{6}$$

where V is the volume at the Hugoniot pressure (V_0 is the initial volume at ambient conditions) and C_V is the heat capacity (for most metals $C_V = 3R/M$). When taking the Grüneisen parameter $\gamma = \gamma_0 (\rho_0/\rho)^n$ with $\gamma_0 = 2.7 \pm 0.2$ and $n = 0.4 \pm 0.1$, the calculated solid Hugoniot temperature is consistent with our measured temperatures up to 171 GPa (Figure 5, shown in the black solid curve). Analysis of the measured longitudinal sound velocity of Fe-9Ni-10Si shows that the sample starts to melt above ~147 GPa and melting is complete at ~183 GPa (Zhang, Sekine, et al., 2016). However, our results for the homogeneous Fe-8Ni-10Si alloy show that it remains solid at 147 GPa. This is because the calculated shock temperature of the previous Fe-9Ni-10Si is higher than this Fe-8Ni-10Si alloy at the same shock pressure due to their different initial states. The Fe-9Ni-10Si sample used in a previous study was a mixture of multiple phases with a low initial density, which can cause a higher shock temperature along the Hugoniot than the single-phase alloy used in this study. Therefore, the homogenous Fe-8Ni-10Si alloy is expected to melt at a higher shock pressure than the Fe-9Ni-10Si alloy mixture. One can see that there is a discontinuity in the measured temperatures between shots D1 to D2 and shots D3 to D4, and the emissivity of shot D2 at 171 GPa is lower than shot D1 at 167 GPa, which indicates that the melting occurred around 171 GPa (Figure 5).

The Hugoniot temperature for liquid Fe-8Ni-10Si can be obtained from the solid state by subtracting a temperature change (ΔT) due to the latent heat of melting ($\Delta T = T_{om}\Delta S/C_V$, ΔS and T_{om} is the entropy change of melting and the onset melting temperature, respectively). We found the entropy change of melting for the Fe-8Ni-10Si alloy was ~0.65($\pm$0.05)R, which matched the measured liquid Hugoniot temperatures of shots D3 and D4 within error, and is slightly lower than the estimated values (0.70–0.75R) for the Fe
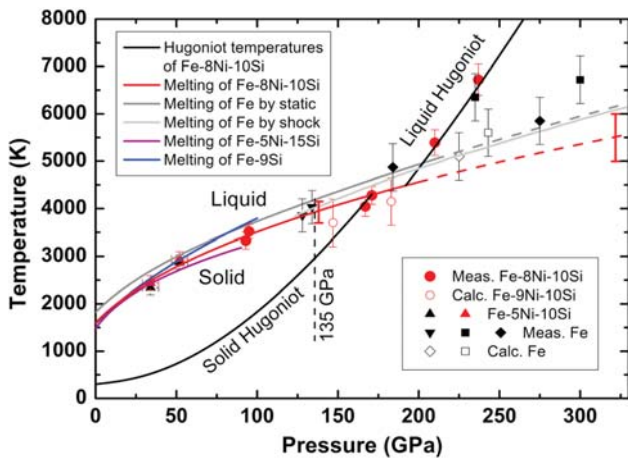
Figure 5. Melting temperatures of the Fe-8Ni-10Si alloy at high pressures and a comparison with the melting curve of pure Fe. Solid circles: Hugoniot and melting temperatures of the Fe-8Ni-10Si alloy from this study; open circles: melting points of the Fe-9Ni-10Si calculated based on sound velocity measurements (Zhang, Sekine, et al., 2016); solid inverted triangles: melting temperatures of Fe at released pressures by pyrometer measurements (Tan et al., 2005); solid squares: melting points of pure Fe based on measured Hugoniot temperatures (Yoo et al., 1993); solid diamonds: melting points of pure Fe reanalyzed by Luo and Ahrens (2004) based on the measured Hugoniot temperatures by Yoo et al. (1993) and Williams et al. (1987) after considering superheating effects; open diamonds (Nguyen & Holmes, 2004) and open squares (Brown & McQueen, 1986): calculated melting points of pure Fe based on sound velocity measurements by shock compression; solid black line: Hugoniot temperature of Fe-8Ni-10Si; red solid and dashed lines: the experimental and extrapolated melting curve of Fe-8Ni-10Si using the Simon equation (this study); and the light gray line: melting curve of pure Fe by shock compression (Nguyen & Holmes, 2004; Tan et al., 2005). The pure Fe and its alloys measured in static diamond anvil cell experiments are also plotted for comparison. Open red and black triangles: lower and upper bounds of the Fe-5Ni-10Si melt (Morard et al., 2011); gray solid and dashed lines: the experimental and extrapolated melting curve of pure Fe using the Simon equation (Anzellini et al., 2013); purple line: the melting curve of Fe-5Ni-15Si (Morard et al., 2011); and the blue line: the melting curve of Fe-9Si (Fischer et al., 2013).

alloys of core materials (Campbell, 2016). The onset melting pressure for Fe-8Ni-10Si alloy is estimated to be at ~171 ± 5 GPa and the complete melting pressure at 192 ± 10 GPa based on the discontinuity between solid and liquid Hugoniot temperatures (Figure 5). This is higher than the previously estimated pressure interval from ~147 GPa to 183 GPa for the Fe-9Ni-10Si alloy mixture, based on sound velocity measurements (Zhang, Sekine, et al., 2016). To determine the melting pressure of the shocked samples accurately, reliable measurements of the longitudinal sound velocity of the samples along the Hugoniot will be needed in the future.

In the thermal emission spectra from the interface in Figure 3, the spectra of shots D1 and D3 exhibit stable plateaus from points A to C during shock compression. However, shot D2 shows a gradual increase instead of a plateau from point B to point C at a Hugoniot pressure of 171 GPa. The temperature and emissivity changes with time for the D2 shot are shown in supporting information Figure S5. The emissivity change is likely caused by the shock-induced partial melting of the sample (Mabire & Héreil, 2002). The emissivity gradually decreases from 0.205 to 0.170 in ~300 ns, while the T_I gradually increases from 3360 K to 3500 K. On the other hand, the spectra of shot D4 at 237 GPa gradually decrease with time after point A, with a slight emissivity increase and temperature decrease (supporting information Figure S5). This is explained by the partially melted LiF at the interface pressure of 131 GPa, which is consistent with previous sound velocity measurements (Liu et al., 2015). The thermal emission at the interface gradually reduces because of the endothermic melting reaction.

3.3. Melting Temperatures of Fe-8Ni-10Si Under High Pressures

The melting temperatures at release pressure (P_R) can be extracted from the shock-induced initial melting phase using a model described in more detail elsewhere (Dai et al., 2009; Tan et al., 2005). There is a constraint relation for melting temperature (T_m) at P_R as illustrated in supporting information Figure S4B, and the equation is

$$T_I \leq T_m \leq T_R \tag{7}$$

The T_m may be approximated to a medium value for most pyrometry experiments (Dai et al., 2009):

$$T_m \cong T_I + (T_I - T_W)/(2\alpha) = (T_I + T_R)/2 \tag{8}$$

The α is about 5–6 in our experiments, so the value for the $(T_I - T_W)/(2\alpha)$ term for the typical pyrometry experiments is much less than T_I. Even if α has a large uncertainty (20–30%), the evaluated T_m is still accurate. The error bars of T_I were directly derived from measurements, while the error bars of T_W and α were evaluated from our measurements and literature data. Thus, the uncertainty of the T_m at P_R was derived from standard error propagations of these parameters with errors. Results for shots D1 and D2 show that the obtained T_m values are slightly higher by ~150 K than the observed T_I at pressure P_R, as listed in Table 3.

Finally, we obtained the melting temperatures at P_R and P_H for the Fe-8Ni-10Si alloy up to ~171 GPa, as shown in Figure 5. Combined with the results for the Fe-5Ni-10Si alloy by LHDAC (Morard et al., 2011), the melting curve up to ~200 GPa was obtained using the Simon equation, wherein T_0 = 1600 K, P_0 = 0 GPa, a = 19.1 ± 4.2, and b = 2.33 ± 0.24 (T in K, P in GPa):

$$(P - P_0)/a = (T/T_0)^b - 1 \tag{9}$$

As illustrated in Figure 5 (red curve), the melting temperature of Fe-8Ni-10Si alloy is 3900 ± 200 K at the CMB pressure of ~136 GPa. The extrapolated melting temperature at the pressure of the ICB (~330 GPa) is 5500 ± 500 K, indicating lower melting temperatures relative to pure iron of ~200–300 (±200) K at the
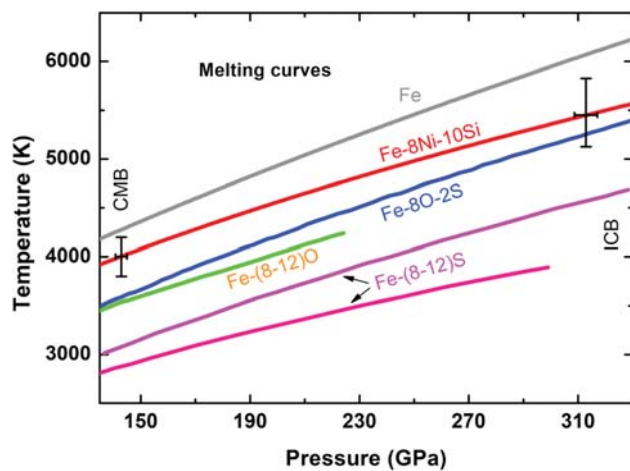
Figure 6. Melting curves of the Fe alloys and the effects of light elements on the melting temperature depression of Fe in the Earth's outer core. The melting curves of the Fe and Fe alloys at high pressures included here are as follows: Fe (Anzellini et al., 2013), Fe-8Ni-10Si (this study), Fe-8O-2S (Huang et al., 2010), Fe-(8–12)O (Boehler, 1993; Komabayashi, 2014; Seagle et al., 2008), and Fe-(8–12)S (Fe-Fe$_3$S system; magenta curve from Kamada et al., 2012, and pink curve from Mori et al., 2017, respectively).

CMB and ~600–800 (±500) K at the ICB, respectively (Anzellini et al., 2013). Compared with the previously determined melting temperatures in the Fe-Ni-Si system, our results are consistent with that of the Fe-5Ni-15Si alloy by LHDAC (Morard et al., 2011) but lower by ~400 K than the data for the Fe-9Si system without Ni at the pressure of the CMB (Fischer et al., 2013). At high pressure-temperature conditions relevant to the Earth's core, the Fe-9Si alloy likely exists as a mixture of hexagonal close packed (hcp) and B2 phases before melting (Fischer et al., 2013), while Fe alloyed with a few wt% Ni and Si likely exhibits a stable hcp phase (Asanuma et al., 2011; Sakai et al., 2011). Thus, the presence of Ni in the Fe-Si alloy can affect the phase stability and may be used to explain the difference in the reported melting curves between Fe-Si and Fe-Ni-Si alloys at high pressures relevant to the Earth's core.

4. Thermal State of the Earth's Core and the Heat Flow Across the CMB

4.1. Density of Fe-8Ni-10Si Along the Adiabatic Core Geotherm

Thermal corrections to the Hugoniot density along a core geotherm are required to check whether a composition represented by Fe-8Ni-10Si matches the core density deficit based on seismic observations, such as the preliminary reference Earth model (PREM; Dziewonski & Anderson, 1981). Based on the measured Hugoniot temperature of the Fe-8Ni-10Si alloy, thermal corrections for the density along a representative core geotherm were refined using the Mie-Grüneisen theory (Brown & McQueen, 1986). The core geotherm we used is based on the measured melting temperature of Fe alloys, the details of which are described in the next section. The density profile of the Fe-8Ni-10Si alloy at the outer core conditions is plotted in supporting information Figure S6. The results show that the slope of the Fe-8Ni-10Si profile along the geotherm is more consistent with the PREM curve than the previous Fe-9Ni-10Si results. The previous data suffered from heterogeneous Fe-9Ni-10Si starting compositions, and the calculated Hugoniot temperature may not be accurate. Because the presence of ~5–10 wt% Ni in Fe would not change its density significantly (Mao et al., 1990; Marsh, 1980), it is thought that the ~10 wt% silicon in Fe-5 wt% Ni alloy is still 1% denser than the PREM density in the whole range of the outer core (supporting information Figure S6). Thus, a silicon content of 11 ± 1 wt% is required in the Fe-Ni-Si system to match PREM, which is in good agreement with the results by static compression (Fischer et al., 2014).

4.2. Melting and the Thermal Structure of the Earth's Core

To evaluate the effect of light elements on the melting temperature depression of Fe, the melting curves of Fe (Anzellini et al., 2013) and Fe alloy candidate core materials are plotted in Figure 6 for comparison, including Fe-8Ni-10Si, Fe-8O-2S (Huang et al., 2010), Fe-(8–12)O (Boehler, 1993; Komabayashi, 2014; Seagle et al., 2008), and Fe-(8–12)S (Kamada et al., 2012; Morard et al., 2014; Mori et al., 2017). The results show that the addition of a light element(s) in Fe such as Si, O, and S depresses the melting temperature of Fe at high pressures by differing magnitudes. Silicon alloyed with iron has a mild effect on melting temperature depression, while oxygen is slightly stronger and sulfur causes the largest melting temperature depression among them. At the CMB, Fe-8Ni-10Si, Fe-(8–12)O, and Fe-(8–12)S have melting temperatures of 3900 K, 3600 K, and 3000 K, respectively, while at the ICB, the melting temperatures are 5500 K, 5400 K, and 4700 K, respectively.

If we assume a linear interpolation for the melting temperatures between the Fe and Fe-light element alloys at the ICB, the compositional dependence on the melting temperature depression (K per wt% of a given light element alloyed with iron) is estimated to be 70 K/wt% for Si, 80 K/wt% for O, and 160 K/wt% for S. For a model core composition of Fe-5Ni-6Si-2S-(1–2.5)O (in wt%; Hirose et al., 2013; Zhang, Sekine, et al., 2016), the melting temperature is ~5300 K at the ICB (T_{ICB}), which is lower than pure Fe by ~900 K. As Figure 7 (black dashed curve) shows, an adiabatic temperature profile in the core is estimated by $T = T_{ICB} (\rho/\rho_{ICB})^\gamma$, with a constant Grüneisen parameter of $\gamma = 1.5$ (Hirose et al., 2013; T is the temperature and ρ_{ICB} is the density of the core at the ICB from the PREM), which leads to a temperature of ~3900 ± 200 K at the CMB. Two types of geothermal models in the lower mantle are considered to constrain the temperature gradient in the D″ region: an
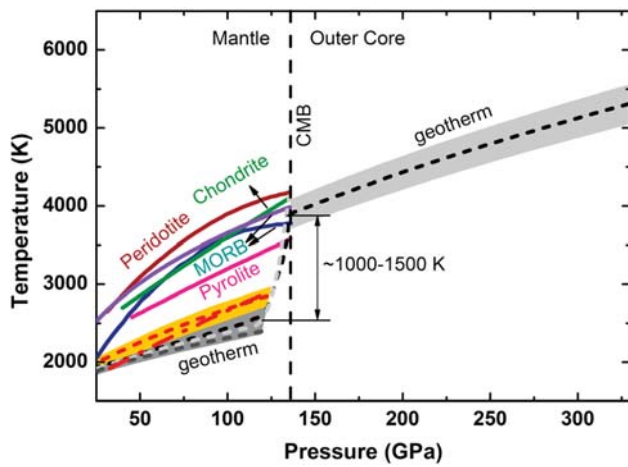
Figure 7. The modeled geotherm of the Earth's outer core and the temperature profile across the core-mantle boundary. Solidus temperatures of representative candidate lower-mantle materials are plotted for comparison. The dashed line above the CMB pressure represents the deduced geotherm of the outer core for a candidate Fe-5Ni-6Si-2S-(1–2.5)O (in wt%), and the gray shaded area indicates the estimated margin of error. Solidus temperatures at the CMB are shown for candidate mantle materials, including natural fertile peridotite (Fiquet et al., 2010); synthetic chondritic primitive mantle (Andrault et al., 2011); natural MORB containing ~0.3 wt% H_2O and traces of CO_2 (navy curve; Andrault et al., 2014); natural MORB containing 2,251 ± 220 ppm H_2O and 483 ± 80 ppm CO_2 (violet curve; Pradhan et al., 2015); and pyrolite containing 400 ppm H_2O (Nomura et al., 2014). The estimated adiabatic geotherm from Brown and Shankland (1981; dark-gray dashed line), Ono (2008; light-gray dashed line), and Katsura et al. (2010; black dashed line), and the superadiabatic geotherm from Anderson (1982; red dashed line) and Matas et al. (2007; red dash-dot line) in the mantle are also plotted, to deduce the temperature gradient at the CMB. The orange and light-black shaded areas indicate the estimated margin of error for the superadiabatic and adiabatic geotherm, respectively. The heat transfer across the CMB (Q_{CMB}) is estimated based on the derived CMB temperature gradient and the extrapolated thermal conductivity of the Fe alloys.

adiabatic geotherm consistent with whole-mantle convection (Brown & Shankland, 1981; Katsura et al., 2010; Ono, 2008) and a superadiabatic geotherm consistent with a layered-mantle convection (Anderson, 1982; Matas et al., 2007) in Figure 7. In the adiabatic model, a mantle boundary temperature at a depth of 2700 km is estimated to be 2600 ± 200 K. Compared to this temperature, the temperature at the top of the outer core yields a thermal boundary layer with a temperature gradient of ΔT ~1300 ± 300 K at a depth interval of ~190 km, which corresponds to a thermal gradient of ~6.8 ± 1.6 K/km in the D'' region. Whereas in the superadiabatic model, a mantle boundary temperature of 2800 ± 200 K at a depth of 2700 km corresponds to a temperature gradient and a thermal gradient of ~1100 ± 300 K and ~5.8 ± 1.6 K/km, respectively, in the D'' region. Therefore, our modeled geotherm of the outer core indicates a thermal gradient of ~5.8–6.8 (±1.6) K/km in the D'' region. We should cautiously note that these estimates for the heat flux and temperature gradients at the CMB highly depend on our understanding of the lower-mantle geotherm models, which remain uncertain.

The onset melting temperatures (solidus) of the lower mantle materials, including peridotite, chondrite, natural mid-oceanic ridge basalt (Morbidelli et al., 2000), and pyrolite, have been compared to the temperature of the core at the pressure conditions of the CMB (Figure 7; Andrault et al., 2011, 2014; Fiquet et al., 2010; Nomura et al., 2014; Pradhan et al., 2015). Previous studies show that the solidus temperatures for the peridotite and chondritic mantle are higher than ~4150 K at CMB pressures (Andrault et al., 2011; Fiquet et al., 2010), which means they are most likely in a solid state at the CMB where the core temperature is ~3900 K. However, the onset melting occurs at around 3800–4000 K for natural MORB containing ~0.2–0.3 wt% of H_2O and traces of CO_2 (Andrault et al., 2014; Pradhan et al., 2015) and even as low as 3570 K for pyrolite containing 400 ppm of H_2O (Nomura et al., 2014), so they may be subjected to local partial melting in the CMB region. These slab materials containing water or volatiles could be brought down to the CMB through subducting slabs that contain hydrous minerals that survive the dehydration processes (Nishi et al., 2014; Ohira et al., 2014; Zhang, Sekine, & He, 2014). The presence of melt due to the partial melting of MORB or pyrolite materials at the lowermost mantle could explain observations of strong lateral seismic heterogeneity at the base of the lower mantle, the variable properties and thickness of the D'' layer, and the ultra-low velocity zones (Garnero, 2000).

4.3. The Heat Flow Across the CMB

Our modeled temperature profile of the outer core can be used to evaluate the temperature gradient and thus the heat flow across the CMB. The heat flow across the CMB is given by (Nimmo, 2015)

$$Q_{CMB} = \oint q \cdot dS \tag{10}$$

where q is the heat flux. For an adiabatic heat flow across the CMB, it may be written as

$$Q_{CMB} = -\oint \kappa \nabla T \cdot dS = 4\pi r^2 \kappa_i \left(\frac{g \gamma T}{\phi} \right)_{CMB} \tag{11}$$

where $r = 3{,}480$ km at the CMB, g is the gravity acceleration of 10.6823 m/s², and ϕ is the seismic parameter with a value of 65.05 km²/s² from the PREM (Dziewonski & Anderson, 1981). Using a Grüneisen parameter of $\gamma = 1.5$ (Hirose et al., 2013), κ_{CMB} of 90–130 W/m/K for our model core composition close to the Fe-12Ni-12.7Si (Fe$_{67.5}$Ni$_{10}$Si$_{22.5}$) and Fe-5.6Si-2.6O (Fe$_{92}$Si$_{10}$O$_8$) alloys (Gomi et al., 2013, 2016; Ohta et al., 2016; Pozzo et al., 2012, 2014; Seagle et al., 2013) and the T_{CMB} of ~3900 K, the Q_{CMB} is estimated to be 13–19 TW (Figure 7). We should note that the estimated Q_{CMB} value highly depends on the reported thermal conductivities of the Fe and Fe alloy at relevant pressure-temperature core conditions, which still remain to be reconciled in different

studies (Dobson, 2016). For example, some previous studies reported a relatively low thermal conductivity of ~30–40 W/m/K in Fe at the relevant pressure-temperature conditions of the CMB (Konôpková et al., 2016; Stacey & Loper, 2007; Zhang et al., 2015), suggesting a low heat flow of ~4–6 TW. The Q_{CMB} value of 13–19 TW inferred from our results and literature values is approximately three to five times higher than the low value estimated from the different thermal conductivities of the core materials.

The heat flow across the lowermost mantle can also be estimated from the thermal conductivity of the mantle materials (κ_{LM}) at CMB conditions using an equation of heat flux $q = \kappa_{LM} \, \Delta T/\delta_{TBL}$, where a thermal boundary layer (δ_{TBL}) with a thickness of ~190 km is in the lowermost mantle (Gomi & Hirose, 2015). The κ_{LM} in the lower mantle is thought to be ~10 W/m/K conventionally (Haigis et al., 2012; Lay et al., 2008; Manthilake et al., 2011) and to be 17–18 W/m/K by recent estimations from the thermal conductivities of post-perovskite and periclase (Imada et al., 2014; Ohta et al., 2012). When taking the ΔT across the CMB as ~1000–1500 K from our study in the δ_{TBL}, it leads to a heat flow of ~8–21 TW. This heat flow based on the κ_{LM} is generally consistent with the high Q_{CMB} value estimated from the κ_{CMB}. Previous estimations for the heat flow across the CMB are also listed in supporting information Table S2 for comparison.

A high Q_{CMB} value of 13–19 TW indicates that the inner core may cool much faster than previously thought, which implies a high initial CMB temperature of above ~4500 K and a young inner core (approximately 0.8–1.2 billion years old) according to a thermal evolution model of the Earth's core (Gomi et al., 2013). A young inner core is generally consistent with a recent palaeomagnetic estimation that there was a sharp increase in the strength of the Earth's palaeomagnetic field around ~1 to 1.5 billion years ago (Biggin et al., 2015). The abrupt change of the magnetic field could indicate initial crystallization of the solid inner core from the cooling liquid outer core. However, it does not support one recent full-vector paleointensity measurement, which shows a magnetic field over 4 billion years old from some of the oldest minerals on Earth, indicating a solid inner core since the beginning of the Earth's formation (Tarduno et al., 2015). Therefore, further studies on the paleomagnetism data and the thermal conductivities of the mantle and core materials are needed to resolve this discrepancy and eventually answer the question about the formation and evolution of the Earth's core.

References

Alboussiere, T., Deguen, R., & Melzani, M. (2010). Melting-induced stratification above the Earth's inner core due to convective translation. *Nature*, *466*(7307), 744–747. https://doi.org/10.1038/nature09257

Alfè, D., Price, G., & Gillan, M. (2002). Iron under Earth's core conditions: Liquid-state thermodynamics and high-pressure melting curve from ab initio calculations. *Physical Review B*, *65*(16), 165118. https://doi.org/10.1103/PhysRevB.65.165118

Allègre, C. J., Poirier, J.-P., Humler, E., & Hofmann, A. W. (1995). The chemical composition of the Earth. *Earth and Planetary Science Letters*, *134*(3-4), 515–526. https://doi.org/10.1016/0012-821X(95)00123-T

Anderson, O. L. (1982). The Earth's core and the phase diagram of iron. *Philosophical Transactions of the Royal Society of London A: Mathematical, Physical and Engineering Sciences*, *306*(1492), 21–35. https://doi.org/10.1098/rsta.1982.0063

Andrault, D., Bolfan-Casanova, N., Nigro, G. L., Bouhifd, M. A., Garbarino, G., & Mezouar, M. (2011). Solidus and liquidus profiles of chondritic mantle: Implication for melting of the Earth across its history. *Earth and Planetary Science Letters*, *304*(1-2), 251–259. https://doi.org/10.1016/j.epsl.2011.02.006

Andrault, D., Pesce, G., Bouhifd, M. A., Bolfan-Casanova, N., Hénot, J.-M., & Mezouar, M. (2014). Melting of subducted basalt at the core-mantle boundary. *Science*, *344*(6186), 892–895. https://doi.org/10.1126/science.1250466

Anzellini, S., Dewaele, A., Mezouar, M., Loubeyre, P., & Morard, G. (2013). Melting of iron at Earth's inner core boundary based on fast X-ray diffraction. *Science*, *340*(6131), 464–466. https://doi.org/10.1126/science.1233514

Aquilanti, G., Trapananti, A., Karandikar, A., Kantor, I., Marini, C., Mathon, O., et al. (2015). Melting of iron determined by X-ray absorption spectroscopy to 100 GPa. *Proceedings of the National Academy of Sciences of the United States of America*, *112*(39), 12,042–12,045. https://doi.org/10.1073/pnas.1502363112

Asanuma, H., Ohtani, E., Sakai, T., Terasaki, H., Kamada, S., Hirao, N., & Ohishi, Y. (2011). Static compression of $Fe_{0.83}Ni_{0.09}Si_{0.08}$ alloy to 374 GPa and $Fe_{0.93}Si_{0.07}$ alloy to 252 GPa: Implications for the Earth's inner core. *Earth and Planetary Science Letters*, *310*(1-2), 113–118. https://doi.org/10.1016/j.epsl.2011.06.034

Asanuma, H., Ohtani, E., Sakai, T., Terasaki, H., Kamada, S., Kondo, T., & Kikegawa, T. (2010). Melting of iron–silicon alloy up to the core–mantle boundary pressure: Implications to the thermal structure of the Earth's core. *Physics and Chemistry of Minerals*, *37*(6), 353–359. https://doi.org/10.1007/s00269-009-0338-7

Biggin, A. J., Piispa, E. J., Pesonen, L. J., Holme, R., Paterson, G. A., Veikkolainen, T., & Tauxe, L. (2015). Palaeomagnetic field intensity variations suggest Mesoproterozoic inner-core nucleation. *Nature*, *526*(7572), 245–248. https://doi.org/10.1038/nature15523

Boehler, R. (1993). Temperatures in the Earth's core from melting-point measurements of iron at high static pressures. *Nature*, *363*(6429), 534–536. https://doi.org/10.1038/363534a0

Brown, J. M., Fritz, J. N., & Hixson, R. S. (2000). Hugoniot data for iron. *Journal of Applied Physics*, *88*(9), 5496–5498. https://doi.org/10.1063/1.1319320

Brown, J. M., & McQueen, R. G. (1986). Phase transitions, Grüneisen parameter, and elasticity for shocked iron between 77 GPa and 400 GPa. *Journal of Geophysical Research*, *91*(B7), 7485–7494. https://doi.org/10.1029/JB091iB07p07485

Brown, J. M., & Shankland, T. J. (1981). Thermodynamic parameters in the Earth as determined from seismic profiles. *Geophysical Journal of the Royal Astronomical Society*, *66*(3), 579–596. https://doi.org/10.1111/j.1365-246X.1981.tb04891.x

Buffett, B. A. (2000). Earth's core and the geodynamo. *Science*, *288*(5473), 2007–2012. https://doi.org/10.1126/science.288.5473.2007

Buffett, B. A. (2003). The thermal state of Earth's core. *Science*, *299*(5613), 1675–1677. https://doi.org/10.1126/science.1081518

Campbell, A. J. (2016). Phase diagrams and thermodynamics of core materials. In H. Terasaki & R. A. Fischer (Eds.), *Deep Earth: Physics and chemistry of the lower mantle and core* (pp. 191–199). Hoboken, NJ: John Wiley.

Dai, C., Hu, J., & Tan, H. (2009). Hugoniot temperatures and melting of tantalum under shock compression determined by optical pyrometry. *Journal of Applied Physics*, *106*(4), 043519. https://doi.org/10.1063/1.3204941

de Koker, N., Steinle-Neumann, G., & Vlček, V. (2012). Electrical resistivity and thermal conductivity of liquid Fe alloys at high *P* and *T*, and heat flux in Earth's core. *Proceedings of the National Academy of Sciences of the United States of America*, *109*(11), 4070–4073. https://doi.org/10.1073/pnas.1111841109

Dobson, D. (2016). Geophysics: Earth's core problem. *Nature*, *534*(7605), 45–45. https://doi.org/10.1038/534045a

Dubrovinsky, L., Dubrovinskaia, N., Langenhorst, F., Dobson, D., Rubie, D., Gessmann, C., et al. (2003). Iron–silica interaction at extreme conditions and the electrically conducting layer at the base of Earth's mantle. *Nature*, *422*(6927), 58–61. https://doi.org/10.1038/nature01422

Dubrovinsky, L., Dubrovinskaia, N., Narygina, O., Kantor, I., Kuznetzov, A., Prakapenka, V., et al. (2007). Body-centered cubic iron-nickel alloy in Earth's core. *Science*, *316*(5833), 1880–1883. https://doi.org/10.1126/science.1142105

Dziewonski, A. M., & Anderson, D. L. (1981). Preliminary reference Earth model. *Physics of the Earth and Planetary Interiors*, *25*(4), 297–356. https://doi.org/10.1016/0031-9201(81)90046-7

Fiquet, G., Auzende, A., Siebert, J., Corgne, A., Bureau, H., Ozawa, H., & Garbarino, G. (2010). Melting of peridotite to 140 gigapascals. *Science*, *329*(5998), 1516–1518. https://doi.org/10.1126/science.1192448

Fischer, R. A. (2016). Melting of Fe alloys and the thermal structure of the core. In H. Terasaki & R. A. Fischer (Eds.), *Deep Earth: Physics and chemistry of the lower mantle and core* (pp. 1–12). Hoboken, NJ: John Wiley. https://doi.org/10.1002/9781118992487.ch1

Fischer, R. A., Campbell, A. J., Caracas, R., Reaman, D. M., Dera, P., & Prakapenka, V. B. (2012). Equation of state and phase diagram of Fe–16Si alloy as a candidate component of Earth's core. *Earth and Planetary Science Letters*, *357*, 268–276.

Fischer, R. A., Campbell, A. J., Caracas, R., Reaman, D. M., Heinz, D. L., Dera, P., & Prakapenka, V. B. (2014). Equations of state in the Fe–FeSi system at high pressures and temperatures. *Journal of Geophysical Research: Solid Earth*, *119*, 2810–2827. https://doi.org/10.1002/2013JB010898

Fischer, R. A., Campbell, A. J., Reaman, D. M., Miller, N. A., Heinz, D. L., Dera, P., & Prakapenka, V. B. (2013). Phase relations in the Fe–FeSi system at high pressures and temperatures. *Earth and Planetary Science Letters*, *373*, 54–64. https://doi.org/10.1016/j.epsl.2013.04.035

Funtikov, A. (2007). Shock compression of iron-silicon alloys with reference to the possible concentration of silicon in the Earth's core. *Izvestiya Physics of the Solid Earth*, *43*(7), 554–558. https://doi.org/10.1134/S106935130707004X

Garnero, E. J. (2000). Heterogeneity of the lowermost mantle. *Annual Review of Earth and Planetary Sciences*, *28*(1), 509–537. https://doi.org/10.1146/annurev.earth.28.1.509

Georg, R. B., Halliday, A. N., Schauble, E. A., & Reynolds, B. C. (2007). Silicon in the Earth's core. *Nature*, *447*(7148), 1102–1106. https://doi.org/10.1038/nature05927

Gomi, H., & Hirose, K. (2015). Electrical resistivity and thermal conductivity of hcp Fe–Ni alloys under high pressure: Implications for thermal convection in the Earth's core. *Physics of the Earth and Planetary Interiors*, *247*, 2–10. https://doi.org/10.1016/j.pepi.2015.04.003

Gomi, H., Hirose, K., Akai, H., & Fei, Y. (2016). Electrical resistivity of substitutionally disordered hcp Fe–Si and Fe–Ni alloys: Chemically-induced resistivity saturation in the Earth's core. *Earth and Planetary Science Letters*, *451*, 51–61. https://doi.org/10.1016/j.epsl.2016.07.011

Gomi, H., Ohta, K., Hirose, K., Labrosse, S., Caracas, R., Verstraete, M. J., & Hernlund, J. W. (2013). The high conductivity of iron and thermal evolution of the Earth's core. *Physics of the Earth and Planetary Interiors*, *224*, 88–103. https://doi.org/10.1016/j.pepi.2013.07.010

Gubbins, D., Sreenivasan, B., Mound, J., & Rost, S. (2011). Melting of the Earth's inner core. *Nature*, *473*(7347), 361–363. https://doi.org/10.1038/nature10068

Haigis, V., Salanne, M., & Jahn, S. (2012). Thermal conductivity of MgO, MgSiO$_3$ perovskite and post-perovskite in the Earth's deep mantle. *Earth and Planetary Science Letters*, *355*, 102–108.

Hao, G., Liu, F., Zhang, D., & Zhang, M. (2007). Optical emission of directly contacted copper/sapphire interface under shock compression of megabar. *Applied Physics Letters*, *90*(26), 261914. https://doi.org/10.1063/1.2751606

Hirose, K., Labrosse, S., & Hernlund, J. (2013). Composition and state of the core. *Annual Review of Earth and Planetary Sciences*, *41*(1), 657–691. https://doi.org/10.1146/annurev-earth-050212-124007

Holland, K. G., & Ahrens, T. J. (1998). Properties of LiF and Al$_2$O$_3$ to 240 GPa for metal shock temperature measurements. In *Properties of Earth and planetary materials at high pressure and temperature* (pp. 335–343). Washington, DC: American Geophysical Union.

Huang, H., Hu, X., Jing, F., Cai, L., Shen, Q., Gong, Z., & Liu, H. (2010). Melting behavior of Fe-O-S at high pressure: A discussion on the melting depression induced by O and S. *Journal of Geophysical Research*, *115*, B05207. https://doi.org/10.1029/2009JB006514

Imada, S., Ohta, K., Yagi, T., Hirose, K., Yoshida, H., & Nagahara, H. (2014). Measurements of lattice thermal conductivity of MgO to core-mantle boundary pressures. *Geophysical Research Letters*, *41*, 4542–4547. https://doi.org/10.1002/2014GL060423

Kamada, S., Ohtani, E., Terasaki, H., Sakai, T., Miyahara, M., Ohishi, Y., & Hirao, N. (2012). Melting relationships in the Fe–Fe$_3$S system up to the outer core conditions. *Earth and Planetary Science Letters*, *359*, 26–33.

Kantor, A. P., Kantor, I. Y., Kurnosov, A. V., Kuznetsov, A. Y., Dubrovinskaia, N. A., Krisch, M., et al. (2007). Sound wave velocities of fcc Fe–Ni alloy at high pressure and temperature by mean of inelastic X-ray scattering. *Physics of the Earth and Planetary Interiors*, *164*(1-2), 83–89. https://doi.org/10.1016/j.pepi.2007.06.006

Katsura, T., Yoneda, A., Yamazaki, D., Yoshino, T., & Ito, E. (2010). Adiabatic temperature profile in the mantle. *Physics of the Earth and Planetary Interiors*, *183*(1-2), 212–218. https://doi.org/10.1016/j.pepi.2010.07.001

Knittle, E., & Jeanloz, R. (1991). Earth's core-mantle boundary: Results of experiments at high pressures and temperatures. *Science*, *251*(5000), 1438–1443. https://doi.org/10.1126/science.251.5000.1438

Komabayashi, T. (2014). Thermodynamics of melting relations in the system Fe-FeO at high pressure: Implications for oxygen in the Earth's core. *Journal of Geophysical Research: Solid Earth*, *119*, 4164–4177. https://doi.org/10.1002/2014JB010980

Kono, Y., Ishikawa, M., & Arima, M. (2007). Effect of H$_2$O released by dehydration of serpentine and chlorite on compressional wave velocities of peridotites at 1 GPa and up to 1000°C. *Physics of the Earth and Planetary Interiors*, *161*(3-4), 215–223. https://doi.org/10.1016/j.pepi.2007.02.005

Konôpková, Z., McWilliams, R. S., Gómez-Pérez, N., & Goncharov, A. F. (2016). Direct measurement of thermal conductivity in solid iron at planetary core conditions. *Nature*, *534*(7605), 99–101. https://doi.org/10.1038/nature18009

Kuwayama, Y., Hirose, K., Sata, N., & Ohishi, Y. (2008). Phase relations of iron and iron-nickel alloys up to 300 GPa: Implications for composition and structure of the Earth's inner core. *Earth and Planetary Science Letters*, *273*(3), 379–385.

Labrosse, S. (2015). Thermal evolution of the core with a high thermal conductivity. *Physics of the Earth and Planetary Interiors*, *247*, 36–55. https://doi.org/10.1016/j.pepi.2015.02.002

Lay, T., Hernlund, J., & Buffett, B. A. (2008). Core-mantle boundary heat flow. *Nature Geoscience*, *1*(1), 25–32. https://doi.org/10.1038/ngeo.2007.44

Li, J., & Fei, Y. (2003). Experimental constraints on core composition. In H. D. Holland & K. K. Turekian (Eds.), *Treatise on geochemistry* (Vol. 2, pp. 521–546). Oxford: Pergamon.

Lin, J.-F., Campbell, A. J., Heinz, D. L., & Shen, G. (2003). Static compression of iron-silicon alloys: Implications for silicon in the Earth's core. *Journal of Geophysical Research*, *108*(B1), 2045. https://doi.org/10.1029/2002JB001978

Lin, J.-F., Heinz, D. L., Campbell, A. J., Devine, J. M., & Shen, G. (2002). Iron-silicon alloy in Earth's core? *Science*, *295*(5553), 313–315. https://doi.org/10.1126/science.1066932

Lin, J. F., Struzhkin, V. V., Sturhahn, W., Huang, E., Zhao, J., Hu, M. Y., et al. (2003). Sound velocities of iron–nickel and iron–silicon alloys at high pressures. *Geophysical Research Letters*, *30*(21), 2112. https://doi.org/10.1029/2003GL018405

Liu, J., Lin, J.-F., Alatas, A., & Bi, W. (2014). Sound velocities of bcc-Fe and $Fe_{0.85}Si_{0.15}$ alloy at high pressure and temperature. *Physics of the Earth and Planetary Interiors*, *233*, 24–32.

Liu, J., Lin, J. F., Alatas, A., Hu, M. Y., Zhao, J., & Dubrovinsky, L. (2016). Seismic parameters of hcp-Fe alloyed with Ni and Si in the Earth's inner core. *Journal of Geophysical Research: Solid Earth*, *121*, 610–623. https://doi.org/10.1002/2015JB012625

Liu, Q., Zhou, X., Zeng, X., & Luo, S. N. (2015). Sound velocity, equation of state, temperature and melting of LiF single crystals under shock compression. *Journal of Applied Physics*, *117*(4), 045901. https://doi.org/10.1063/1.4906558

Lord, O. T., Wood, I. G., Dobson, D. P., Vočadlo, L., Wang, W., Thomson, A. R., et al. (2014). The melting curve of Ni to 1 Mbar. *Earth and Planetary Science Letters*, *408*, 226–236. https://doi.org/10.1016/j.epsl.2014.09.046

Luo, S.-N., & Ahrens, T. J. (2004). Shock-induced superheating and melting curves of geophysically important minerals. *Physics of the Earth and Planetary Interiors*, *143–144*, 369–386.

Mabire, C., & Héreil, P. L. (2002). Shock induced melting of lead (experimental study). *AIP Conference Proceedings*, *620*(1), 229–232.

Manthilake, G. M., de Koker, N., Frost, D. J., & Mccammon, C. A. (2011). Lattice thermal conductivity of lower mantle minerals and heat flux from Earth's core. *Proceedings of the National Academy of Sciences of the United States of America*, *108*(44), 17,901–17,904. https://doi.org/10.1073/pnas.1110594108

Mao, Z., Lin, J.-F., Liu, J., Alatas, A., Gao, L., Zhao, J., & Mao, H.-K. (2012). Sound velocities of Fe and Fe-Si alloy in the Earth's core. *Proceedings of the National Academy of Sciences of the United States of America*, *109*(26), 10,239–10,244. https://doi.org/10.1073/pnas.1207086109

Mao, H., Wu, Y., Chen, L., Shu, J., & Jephcoat, A. P. (1990). Static compression of iron to 300 GPa and $Fe_{0.8}Ni_{0.2}$ alloy to 260 GPa: Implications for composition of the core. *Journal of Geophysical Research*, *95*(B13), 21,737–21,742. https://doi.org/10.1029/JB095iB13p21737

Marsh, S. P. (1980). *LASL shock Hugoniot data*. Berkeley: Univeisity of California Press.

Matas, J., Bass, J., Ricard, Y., Mattern, E., & Bukowinski, M. (2007). On the bulk composition of the lower mantle: Predictions and limitations from generalized inversion of radial seismic profiles. *Geophysical Journal International*, *170*(2), 764–780. https://doi.org/10.1111/j.1365-246X.2007.03454.x

McDonough, W. (2003). Compositional model for the Earth's core. In H. D. Holland & K. K. Turekian (Eds.), *Treatise on geochemistry*, (Vol. 2, pp. 547–568). Oxford: Pergamon. https://doi.org/10.1016/B0-08-043751-6/02015-6

McQueen, R. G., Marsh, S. P., Taylor, J. W., Fritz, J. N., & Carter, W. J. (1970). The equation of state of solids from shock wave studies. In R. Kinslow (Ed.), *High-velocity impact phenomena* (pp. 293–417). San Diego, CA: Academic Press. https://doi.org/10.1016/B978-0-12-408950-1.50012-4

Morard, G., Andrault, D., Antonangeli, D., & Bouchet, J. (2014). Properties of iron alloys under the Earth's core conditions. *Comptes Rendus Geoscience*, *346*(5-6), 130–139. https://doi.org/10.1016/j.crte.2014.04.007

Morard, G., Andrault, D., Guignot, N., Siebert, J., Garbarino, G., & Antonangeli, D. (2011). Melting of Fe-Ni-Si and Fe-Ni-S alloys at megabar pressures: Implications for the core-mantle boundary temperature. *Physics and Chemistry of Minerals*, *38*(10), 767–776. https://doi.org/10.1007/s00269-011-0449-9

Morbidelli, A., Chambers, J., Lunine, J., Petit, J.-M., Robert, F., Valsecchi, G., & Cyr, K. (2000). Source regions and timescales for the delivery of water to the Earth. *Meteoritics and Planetary Science*, *35*(6), 1309–1320. https://doi.org/10.1111/j.1945-5100.2000.tb01518.x

Mori, Y., Ozawa, H., Hirose, K., Sinmyo, R., Tateno, S., Morard, G., & Ohishi, Y. (2017). Melting experiments on Fe–Fe3S system to 254 GPa. *Earth and Planetary Science Letters*, *464*(Supplement C), 135–141.

Nellis, W., & Yoo, C. (1990). Issues concerning shock temperature measurements of iron and other metals. *Journal of Geophysical Research*, *95*(B13), 21,749–21,752. https://doi.org/10.1029/JB095iB13p21749l

Nguyen, J. H., & Holmes, N. C. (2004). Melting of iron at the physical conditions of the Earth's core. *Nature*, *427*(6972), 339–342. https://doi.org/10.1038/nature02248

Nimmo, F. (2015). Energetics of the core. In G. Schubert (Ed.), *Treatise on geochemistry* (Vol. 8, pp. 27–55). Oxford: Elsevier. https://doi.org/10.1016/B978-0-444-53802-4.00139-1

Nishi, M., Irifune, T., Tsuchiya, J., Tange, Y., Nishihara, Y., Fujino, K., & Higo, Y. (2014). Stability of hydrous silicate at high pressures and water transport to the deep lower mantle. *Nature Geoscience*, *7*(3), 224–227. https://doi.org/10.1038/ngeo2074

Nomura, R., Hirose, K., Uesugi, K., Ohishi, Y., Tsuchiyama, A., Miyake, A., & Ueno, Y. (2014). Low core-mantle boundary temperature inferred from the solidus of pyrolite. *Science*, *343*(6170), 522–525. https://doi.org/10.1126/science.1248186

Ohira, I., Ohtani, E., Sakai, T., Miyahara, M., Hirao, N., Ohishi, Y., & Nishijima, M. (2014). Stability of a hydrous δ-phase, $AlOOH–MgSiO_2(OH)_2$, and a mechanism for water transport into the base of lower mantle. *Earth and Planetary Science Letters*, *401*, 12–17. https://doi.org/10.1016/j.epsl.2014.05.059

Ohta, K., Kuwayama, Y., Hirose, K., Shimizu, K., & Ohishi, Y. (2016). Experimental determination of the electrical resistivity of iron at Earth's core conditions. *Nature*, *534*(7605), 95–98. https://doi.org/10.1038/nature17957

Ohta, K., Yagi, T., Taketoshi, N., Hirose, K., Komabayashi, T., Baba, T., et al. (2012). Lattice thermal conductivity of $MgSiO_3$ perovskite and post-perovskite at the core–mantle boundary. *Earth and Planetary Science Letters*, *349*, 109–115.

Ono, S. (2008). Experimental constraints on the temperature profile in the lower mantle. *Physics of the Earth and Planetary Interiors*, *170*(3-4), 267–273. https://doi.org/10.1016/j.pepi.2008.06.033

Poirier, J.-P. (1994). Light elements in the Earth's outer core: A critical review. *Physics of the Earth and Planetary Interiors*, *85*(3-4), 319–337. https://doi.org/10.1016/0031-9201(94)90120-1

Pozzo, M., Davies, C., Gubbins, D., & Alfè, D. (2012). Thermal and electrical conductivity of iron at Earth's core conditions. *Nature*, *485*(7398), 355–358. https://doi.org/10.1038/nature11031

Pozzo, M., Davies, C., Gubbins, D., & Alfè, D. (2013). Transport properties for liquid silicon-oxygen-iron mixtures at Earth's core conditions. *Physical Review B*, *87*(1), 014110. https://doi.org/10.1103/PhysRevB.87.014110

Pozzo, M., Davies, C., Gubbins, D., & Alfè, D. (2014). Thermal and electrical conductivity of solid iron and iron–silicon mixtures at Earth's core conditions. *Earth and Planetary Science Letters*, *393*, 159–164.

Pradhan, G. K., Fiquet, G., Siebert, J., Auzende, A.-L., Morard, G., Antonangeli, D., & Garbarino, G. (2015). Melting of MORB at core–mantle boundary. *Earth and Planetary Science Letters*, *431*, 247–255. https://doi.org/10.1016/j.epsl.2015.09.034

Rainey, E. (2014). The thermal conductivity of the Earth's lower mantle and implications for heat flow at the core-mantle boundary, Ph.D. UCLA: Geophysics & Space Physics 0406.

Ricolleau, A., Fei, Y., Corgne, A., Siebert, J., & Badro, J. (2011). Oxygen and silicon contents of Earth's core from high pressure metal–silicate partitioning experiments. *Earth and Planetary Science Letters*, *310*(3-4), 409–421. https://doi.org/10.1016/j.epsl.2011.08.004

Sakai, T., Ohtani, E., Hirao, N., & Ohishi, Y. (2011). Stability field of the hcp-structure for Fe, Fe-Ni, and Fe-Ni-Si alloys up to 3 Mbar. *Geophysical Research Letters*, *38*, L09302. https://doi.org/10.1029/2011GL047178

Seagle, C. T., Cottrell, E., Fei, Y., Hummer, D. R., & Prakapenka, V. B. (2013). Electrical and thermal transport properties of iron and iron-silicon alloy at high pressure. *Geophysical Research Letters*, *40*, 5377–5381. https://doi.org/10.1002/2013GL057930

Seagle, C., Heinz, D., Campbell, A., Prakapenka, V., & Wanless, S. (2008). Melting and thermal expansion in the Fe–FeO system at high pressure. *Earth and Planetary Science Letters*, *265*(3-4), 655–665. https://doi.org/10.1016/j.epsl.2007.11.004

Smirnov, N. A. (2011). Ab initio calculations of the thermodynamic properties of LiF crystal. *Physical Review B*, *83*(1), 014109. https://doi.org/10.1103/PhysRevB.83.014109

Sola, E., & Alfe, D. (2009). Melting of iron under Earth's core conditions from diffusion Monte Carlo free energy calculations. *Physical Review Letters*, *103*(7), 078501. https://doi.org/10.1103/PhysRevLett.103.078501

Stacey, F. D., & Anderson, O. L. (2001). Electrical and thermal conductivities of Fe–Ni–Si alloy under core conditions. *Physics of the Earth and Planetary Interiors*, *124*(3-4), 153–162. https://doi.org/10.1016/S0031-9201(01)00186-8

Stacey, F. D., & Loper, D. E. (2007). A revised estimate of the conductivity of iron alloy at high pressure and implications for the core energy balance. *Physics of the Earth and Planetary Interiors*, *161*(1-2), 13–18. https://doi.org/10.1016/j.pepi.2006.12.001

Takafuji, N., Hirose, K., Mitome, M., & Bando, Y. (2005). Solubilities of O and Si in liquid iron in equilibrium with (Mg, Fe) SiO_3 perovskite and the light elements in the core. *Geophysical Research Letters*, *32*, L06313. https://doi.org/10.1029/2005GL022773

Tan, H., Dai, C., Zhang, L., & Xu, C. (2005). Method to determine the melting temperatures of metals under megabar shock pressures. *Applied Physics Letters*, *87*(22), 221905. https://doi.org/10.1063/1.2043248

Tarduno, J. A., Cottrell, R. D., Davis, W. J., Nimmo, F., & Bono, R. K. (2015). A Hadean to Paleoarchean geodynamo recorded by single zircon crystals. *Science*, *349*(6247), 521–524. https://doi.org/10.1126/science.aaa9114

Tsuno, K., Frost, D. J., & Rubie, D. C. (2013). Simultaneous partitioning of silicon and oxygen into the Earth's core during early Earth differentiation. *Geophysical Research Letters*, *40*, 66–71. https://doi.org/10.1029/2012GL054116

Van der Hilst, R., De Hoop, M., Wang, P., Shim, S.-H., Ma, P., & Tenorio, L. (2007). Seismostratigraphy and thermal structure of Earth's core-mantle boundary region. *Science*, *315*(5820), 1813–1817. https://doi.org/10.1126/science.1137867

Williams, Q., Jeanloz, R., Bass, J., Svendsen, B., & Ahrens, T. J. (1987). The melting curve of iron to 250 gigapascals: A constraint on the temperature at Earth's center. *Science*, *236*(4798), 181–182. https://doi.org/10.1126/science.236.4798.181

Yoo, C. S., Holmes, N. C., Ross, M., Webb, D. J., & Pike, C. (1993). Shock temperatures and melting of iron at Earth core conditions. *Physical Review Letters*, *70*(25), 3931–3934. https://doi.org/10.1103/PhysRevLett.70.3931

Zhang, P., Cohen, R., & Haule, K. (2015). Effects of electron correlations on transport properties of iron at Earth's core conditions. *Nature*, *517*(7536), 605–607. https://doi.org/10.1038/nature14090

Zhang, D., Jackson, J. M., Zhao, J., Sturhahn, W., Alp, E. E., Hu, M. Y., et al. (2016). Temperature of Earth's core constrained from melting of Fe and $Fe_{0.9}Ni_{0.1}$ at high pressures. *Earth and Planetary Science Letters*, *447*, 72–83. https://doi.org/10.1016/j.epsl.2016.04.026

Zhang, Y., Sekine, T., & He, H. (2014). A new interpretation of decomposition products of serpentine under shock compression. *American Mineralogist*, *99*(11-12), 2374–2377. https://doi.org/10.2138/am-2014-5021

Zhang, Y., Sekine, T., He, H., Yu, Y., Liu, F., & Zhang, M. (2014). Shock compression of Fe-Ni-Si system to 280 GPa: Implications for the composition of the Earth's outer core. *Geophysical Research Letters*, *41*, 4554–4559. https://doi.org/10.1002/2014GL060670

Zhang, Y., Sekine, T., He, H., Yu, Y., Liu, F., & Zhang, M. (2016). Experimental constraints on light elements in the Earth's outer core. *Scientific Reports*, *6*, 22473. https://doi.org/10.1038/srep22473

Zhao, W.-G., Zhou, X.-M., Li, J.-B., Li, J., & Zeng, X.-L. (2014). Thermal conductivity of shocked LiF single crystal measurement by liquid sandwich method. *Journal of Atomic and Molecular Physics*, *31*, 140–148.

Zhou, X., Nellis, W. J., Li, J., Li, J., Zhao, W., Liu, X., et al. (2015). Optical emission, shock-induced opacity, temperatures, and melting of $Gd_3Ga_5O_{12}$ single crystals shock-compressed from 41 to 290 GPa. *Journal of Applied Physics*, *118*(5), 055903. https://doi.org/10.1063/1.4928081